



Supported Pt, Pd and Au nanoparticle anode catalysts for anion-exchange membrane fuel cells with glycerol and crude glycerol fuels

Zhiyong Zhang¹, Le Xin¹, Ji Qi, David J. Chadderton, Wenzhen Li*

Department of Chemical Engineering, Michigan Technological University, Houghton, MI 49931, USA

ARTICLE INFO

Article history:

Received 26 October 2012

Received in revised form 21 January 2013

Accepted 26 January 2013

Available online 5 February 2013

Keywords:

Nanoparticle

Electro-oxidation

Crude glycerol

Alkaline electrolyte

Fuel cell

ABSTRACT

Carbon supported Pt, Pd, and Au nanoparticles (NPs) catalysts with small diameters (2.4–3.5 nm) were prepared through a solution-phase reduction method, and applied as the model catalysts for electro-oxidation of both high-purity glycerol and biodiesel-derived crude glycerol. The half cell investigations showed that Pt/C has the highest activity in the low potential range, which can be further facilitated at elevated temperatures. The anion-exchange membrane fuel cells (AEMFCs) investigations demonstrated no obvious drop in peak power density on Pt/C anode, when the fuel was switched from high-purity glycerol to crude glycerol, indicating a good stability of the Pt/C against poisoning/deactivation from the impurities in crude glycerol. The tests also showed that on all these three model catalysts, a volcano-type relationship exists between the fuel cell performance and crude glycerol concentration at a fixed KOH concentration, while with a given crude glycerol concentration, the performance monotonically increased with the KOH concentration increasing. The highest performances were achieved with 6.0 M KOH + 1.0 M crude glycerol at 80 °C, which are 184.2, 93.9, and 50.1 mW cm⁻² on Pt/C, Pd/C, and Au/C anodes, respectively.

© 2013 Elsevier B.V. All rights reserved.

1. Introduction

The energy crisis rising from the depletion of fossil fuels has been growing up to an unavoidable concern that significantly affects the growth of the economy and the sustainability of humanity [1–4]. In 2011, the world consumed a total energy of 12274.6 million tonnes oil equivalent, 87% of which are supplied by fossil fuels [5]. The demand of energy lays a heavy burden on the dwindling petroleum resources, and raises the current crude oil price 5-fold higher than that in 1990s [6]. In addition, the current main stream energy device, internal combustion engine, is not only struggling with low efficiency (<13%) [7], but also devastating the natural environment by emitting pollutants (NO_x, SO_x, and CO) and greenhouse gas (CO₂) far more than that can be recovered in atmosphere [8]. The large concerns associated with the economy, environment, and sustainability, greatly spurred the development of more renewable energy resources and more efficient energy conversion techniques [9–11].

Recently, direct alcohol fuel cells (DAFCs) have been recognized as a promising alternative electrical power generation device

to meet the humanity's energy demands [12–14]. Compared to H₂ fuel, liquid alcohol fuels are easy to store and transport, and can be derived from annually renewable biomass feedstocks. In a DAFC, the chemical energy stored in the fuel is directly converted into electrical energy without the limitation of Carnot's theorem. Therefore, the theoretical efficiency is usually >90% [15,16]. In an anion-exchange membrane – direct alcohol fuel cell, the cell performance is further improved as both the anode and cathode reactions are significantly enhanced by the better mass transfer and lower adsorption of spectator charged species [17]. In addition, the products of an AEM-DAFC remain in the aqueous solution, with zero environmental impact. Numerous studies have been carried out in anion-exchange membrane fuel cells (AEMFCs) with different biorenewable alcohol fuels, including methanol [18–21], ethanol [22–24], ethylene glycerol [25,26], and glycerol [16,27–32]. Recently, Prakash et al. reported a peak power density of 168 mW cm⁻² on a methanol-fed PtRu anode (3 mg_{PtRu} cm⁻²) AEMFC at 90 °C [20]. Bianchini et al. also observed a peak power density of 160 mW cm⁻² on an ethanol-fed Pd-(Ni-Zn-P)/C anode (1 mg_{Pd} cm⁻²) AEMFC at 80 °C [33]. However, the toxicity of methanol and high volatility of ethanol, along with their low flash points remain critical issues before their wide application in AEMFCs.

Glycerol has attracted great research interests as a non-toxic, non-volatile, and non-flammable biorenewable alcohol fuel.

* Corresponding author. Tel.: +1 906 487 2298; fax: +1 906 487 3213.

E-mail addresses: wzli@mtu.edu, liwenzhen@gmail.com (W. Li).

¹ These authors contributed equally to this work.

Different from biomethanol and bioethanol, which are obtained from the microorganism fermentation process of biomass, biomass derived glycerol is mainly obtained as a waste byproduct in the production of biodiesel via a transesterification reaction [34]. As a result, biodiesel derived glycerol now can be obtained at relatively lower market price (0.74–0.89 US\$ gal⁻¹ for crude glycerol, vs. 1.34 US\$ gal⁻¹ for methanol and 3.15 US\$ gal⁻¹ for ethanol). In addition, with the highly active triol structure, glycerol demonstrates a high volumetric energy density of 6.4 kWh L⁻¹ [16,31]. Various studies have been carried out in the electro-oxidation of glycerol on Pt, Pd, and Au based catalysts. In AEMFC studies, Matsuoka et al. first reported a peak power density of ~ 7 mW cm⁻² at 50 °C, using PtRu as the anode catalyst [27]. Ilie et al. investigated the membrane electrode assembly (MEA) fabrication methods and reaction condition (fuel concentration, flow rate, etc.) and obtained an optimized peak power density of ~ 24 mW cm⁻² with Pt and Pt-based bimetallic anode catalysts at 60 °C [30]. Bianchini's group reported peak power densities of ~ 79 and 118 mW cm⁻² on Pd/CNT [28] and Pd-(Ni-Zn-P)/C [29] anode catalysts, respectively. Recently, based on a simple nanocapsule method, our group successfully prepared highly active Pt/C and Au/C catalyst, and demonstrated exciting peak power densities of ~ 125 and 58 mW cm⁻² on Pt/C and Au/C anode AEMFCs [16,31,32]. However, all of these studies were based on the high price petrochemical derived high purity glycerol (99.8%, usually ~ 40 US\$ L⁻¹ or ~ 150 US\$ gal⁻¹ from the main chemical suppliers). As the purification of crude glycerol is prohibitively expensive [35], it is usually sold with many impurities, including methanol, fatty acids (usually in the form of soaps), transesterification catalysts residues (as ash content), a variety of element such as K, Ca, Mg, Hg, P, S, As, etc. (as both dissolved and undissolved salts) [36]. Due to the concerns about the contamination and poisoning of these impurities to the fuel cell system, little investigation has been performed on the AEMFC with direct crude glycerol fuels. To directly utilize crude glycerol as a fuel for the AEMFCs, there is a clear need to first investigate the intrinsic activity of monometallic Pt, Pd, and Au catalysts toward glycerol oxidation and demonstrate their performances as the anode catalysts with crude glycerol fuel, so as to further develop more efficient multi-metallic catalysts.

In the present work, a simple organic solution-phase reduction method [37–39] was applied to prepare the carbon supported Pt, Pd, and Au nanoparticle as the model catalysts. The catalytic activities of these as-prepared catalysts toward glycerol electro-oxidation were first compared in half cell at different temperature. Based on the half cell test results, these catalysts were further applied as the anode catalysts in AEMFCs. The effects on the performance with soybean biodiesel derived crude glycerol were evaluated at 80 °C. It is demonstrated that Pt/C anode AEMFC holds the highest performance with high purity glycerol fuel, which also shows no obvious performance loss when switching to crude glycerol fuel. Fed with 6.0 M KOH + 1.0 M crude glycerol, the peak power density on Pt/C anode AEMFC can reach 184.2 mW cm⁻², while that on Pd/C and Au/C anode AEMFCs can also reach 93.9 and 50.1 mW cm⁻².

2. Experimental

2.1. Chemicals

Pt(acac)₂, Pd(acac)₂, LiBET₃H (1 M in THF), 1-octadecene, and benzyl ether were purchased from Acros Organics. Oleylamine is purchased from Aldrich Chemistry. Oleic acid and high purity glycerol (99.8%) were purchased from Fisher Chemical. AuCl₃ was purchased from Alfa Aesar. Crude glycerol (88%, a byproduct from soy biodiesel manufacturing) was obtained from Kingdom Bio Solutions Inc. All the chemicals were used as purchased without further purification.

2.2. Preparation of Pt/C, Pd/C, and Au/C catalysts

All catalysts were synthesized through a modified organic solution phase reduction method [15,31,32,40]. For the preparation of Pt/C (40 wt%), 196.7 mg of Pt(acac)₂ (0.5 mmol), 200 μ L of oleylamine, and 200 μ L of oleic acid were first dissolved in a mixture of 146.3 mg Vulcan XC-72R carbon black and 40 mL of benzyl ether at 60 °C under a N₂ protection. As the temperature was increased to 120 °C, 1.0 mL of LiBET₃H was quickly injected into the system. The temperature was held for 30 min, and then slowly increased to 180 °C and held for an additional 30 min. Pd/C (40 wt%) was prepared through a similar procedure. 152.3 mg of Pd(acac)₂ (0.5 mmol) and 79.8 mg of carbon black were mixed in 40 mL benzyl ether solvent, and was rapidly heated to 100 °C in a N₂ atmosphere. As the temperature reached 100 °C, 200 μ L of oleylamine and 200 μ L of oleic acid were injected into the system, followed by quick injection of 1.0 mL LiBET₃H. The temperature was held for 20 min, and then slowly raised to 180 °C and held for an additional 30 min. To prepare Au/C (40 wt%), 151.7 mg of AuCl₃ (0.5 mmol) was mixed with 16 mL of 1-octadecene and 4 mL of oleylamine under a nitrogen blanket. The system was then rapidly heated to 80 °C, subsequently followed by a quick injection of 1.5 mL LiBET₃H. After holding the temperature for 10 min, the solution was cooled down to room temperature and mixed with 148.0 mg of carbon black. All the final products were collected by filtration, washed with copious ethanol, and dried in vacuum oven at 50 °C overnight.

2.3. Physical characterizations

The morphology, nanostructure and metal loading of the catalysts were analyzed by transmission electron microscopy (TEM), X-ray diffraction (XRD), and induced couple plasma-atomic emission spectroscopy (ICP-AES). The TEM characterizations were performed on a JEOL JEM-4000FX with an operation voltage of 200 kV. The XRD patterns were collected on a Scintag XDS-2000 θ/θ Diffractometer with Cu K α radiation ($\lambda = 1.5406$ Å), with a tube current of 35 mA and a tube voltage of 45 kV. The ICP-AES was performed after dissolving 10 mg of the catalyst into freshly prepared aqua regia (a strong corrosive acid formed by mixing concentrated nitric acid and hydrochloric acid with the volume ratio of 1:3), in order to analyze the metal loading.

2.4. Half cell tests

Half cell tests were conducted in a conventional three-electrode-cell setup (electrolyte cell AFCELL3, Pine Instrument), with a glassy carbon working electrode, a Hg/HgO/1.0 M KOH electrode, and a Pt wire counter electrode. The cell is covered by a water jacket, which enables the system to be thermostated at 25, 50, or 60 °C during the test. Prior to tests, all the electrolytes were deaerated by purging with high purity N₂ for 30 min. All potentials in the present study were given vs. Hg/HgO/1.0 M KOH electrode (0.140 V vs. NHE) [41] unless otherwise mentioned. Before each test, 2.0 mg of catalyst was dispersed in 1.0 mL of isopropanol by bath ultrasonication until no aggregation was visible to the eye. The working electrode was prepared by dropping 20 μ L of the ink on the glassy carbon electrode, which yielded a catalyst loading of ~ 40 μ g_{metal} cm⁻². 10 μ L of 0.05 wt% AS4 (Tokuyama) ionomer solution was added on top to affix the catalyst. A 10-cycle cyclic voltammetry (CV) test was performed on each catalyst in 1.0 M KOH with a sweep rate of 50 mV s⁻¹, 25 °C. The stable polarization curve obtained from the last cycle was used to calculate the electrochemical surface area (ECSA). For Pt/C catalyst, the ECSA was evaluated based on hydrogen desorption peak with the Pt pseudo-capacity of 0.210 mC cm⁻². The ECSA of Pd/C was obtained from the PdO reduction peak to avoid the multilayer hydrogen adsorption/absorption

issue on Pd. A pseudo-capacity of 0.405 mC cm^{-2} for the reduction of a monolayer PdO was used according to our previous work [15,39]. Due to the weak hydrogen adsorption/desorption on Au surface, the ECSA of Au/C was also measured from the reduction peak at $\sim 0.13 \text{ V}$, with a pseudo-capacity of 0.386 mC cm^{-2} for the reduction of the oxide formed on Au surface [32,42]. To study the glycerol oxidation activity, 10-cycle-CV tests were performed on all the three catalysts in $1.0 \text{ M KOH} + 0.5 \text{ M glycerol}$ at the same sweep rate, at 25°C . A linear sweep voltammetry (LSV) on each catalyst with a sweep rate of 1 mV s^{-1} and a rotation rate of 2500 rpm was performed at different temperatures. The onset potential of glycerol oxidation is defined as the potential where the inflection is observed on the quasi-steady state polarization curve. The linear polarization plot at 25°C was also used to study the Tafel slope and turnover frequency (TOF). The Tafel plot was achieved by plotting the potential against the logarithm of current density, which is described by the following equation [15,43]:

$$\eta = 2.303 \frac{RT}{\alpha n F} \log \left(\frac{j}{j_0} \right) \quad (1)$$

here, η is the potential, α is the charge transfer coefficient, n is the number of electrons transferred in the reaction, j_0 is the exchange current density, and j is the current density obtained in the quasi-steady state scan. The quantity preceding the logarithm is defined as Tafel slope $b = 2.303(RT/\alpha n F)$.

The turnover frequency (TOF) of electrons is defined as follows [44]:

$$\text{TOF} = \frac{j}{e N_s} \quad (2)$$

where N_s is the active surface atom density that was calculated from the ECSA of the catalyst.

2.5. MEA fabrications and AEMFC tests

The MEA with anode, solid electrolyte membrane, and cathode was mechanically sandwiched, and has an active cross-sectional area of 5 cm^2 . At the anode, catalyst ink containing 90 wt% of Pt/C, Pd/C, or Au/C catalyst and 10 wt% of Teflon was airbrushed onto a carbon cloth liquid diffusion layer, to obtain a catalyst loading of $1.0 \text{ mg}_{\text{metal}} \text{ cm}^{-2}$. At the cathode, 70 wt% of a commercial non-Pt group metal (PGM) HYPERMECTM catalyst (Fe-Cu-N₄/C, Acta) was blended with 30 wt% AS-4 anion conductive ionomer (Tokuyama), and sprayed directly onto the A201 anion-exchange membrane (Tokuyama). A 25CC carbon paper (SGL Group) was placed to cover the cathode catalyst as a gas diffusion layer. The performance of AEMFC was evaluated at 80°C , with a high purity glycerol or crude glycerol + KOH solution and high purity O₂ (99.999%) at a constant flow rate of 0.4 L min^{-1} under 30 psi back pressure.

3. Results and discussions

3.1. Physical characterizations

The XRD patterns of Pt/C, Pd/C, and Au/C catalysts were collected in the range from 15 to 100° , and are shown in Fig. 1. All of them displayed a typical face-centered cubic (FCC) pattern, with the diffraction peaks at $\sim 39^\circ$, 46° , 67° , and 80° assigned to the corresponding (1 1 1), (2 0 0), (2 2 0), and (3 1 1), respectively. The peak around 25° in all the catalysts is referred to the graphite (0 0 2) facet of the carbon support. The average crystal size of each catalyst is calculated based on the corresponding (2 2 0) diffraction peak, using the Debye–Scherrer formula [45,46]:

$$L = \frac{0.9 \lambda_{K\alpha}}{B_{2\theta} \cos \theta_{\max}} \quad (3)$$

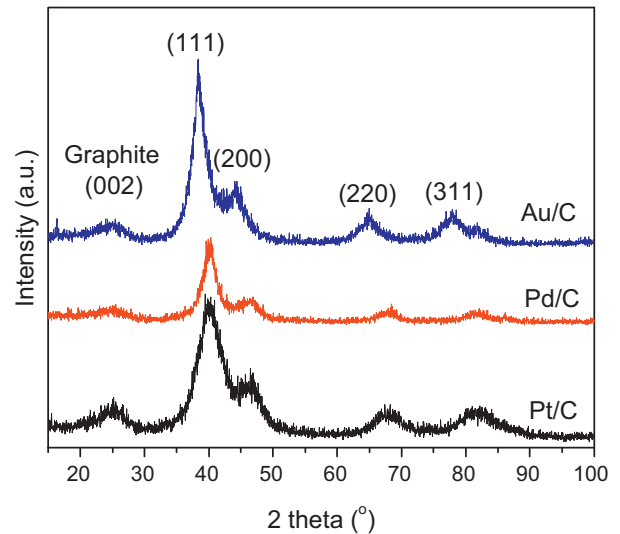


Fig. 1. XRD patterns of Pt/C, Pd/C, and Au/C catalysts.

where L is the mean crystal size, λ is the wavelength of the X-ray (1.5406 \AA), $B_{2\theta}$ is the full width at half-maximum of the peak (rad), and θ_{\max} is the Bragg angle (rad). The results yielded from Eq. (3) are summarized in Table 1, which are 1.9, 2.5, and 3.4 nm for Pt/C, Pd/C, and Au/C catalysts, respectively.

The typical TEM images of Pt/C, Pd/C, and Au/C, and their corresponding histograms are shown in Fig. 2. It is shown that most of the catalysts are round in shape and are uniformly dispersed on carbon support with little agglomeration. The average particle sizes evaluated from TEM images are 2.4 , 3.4 , and 3.5 nm for Pt/C, Pd/C, and Au/C catalysts, which are in good agreement with the results from XRD analysis. The histograms of particle sizes of these catalysts are counted from 100 randomly chosen particles in an arbitrarily chosen area, and show narrow size distributions for all the catalysts, indicating a good morphology control of the nanocapsule method for these three metal catalysts. The metal loadings of Pt/C, Pd/C, and Au/C catalysts evaluated by the ICP-AES (Table 2) are 38%, 37%, and 35%, respectively, which are very close to the setting ratio of 40%, indicating all the metal precursors were fully reduced by the present synthesis method.

3.2. Half cell tests

The cyclic voltammograms (CV) obtained on Pt/C, Pd/C, and Au/C catalysts in N₂-saturated 1.0 M KOH at 25°C are shown in Fig. 3. In the CV plot of Pt/C, the anodic peak from -0.9 to -0.45 V is assigned to the hydrogen underpotential desorption peak, which is immediately followed by the OH[−] adsorption peak [47–50]. However, in the CV plot of Pd/C, the OH[−] adsorption starts at even negative potentials, which covers the hydrogen underpotential desorption peak and give rise to the small peak at $\sim -0.35 \text{ V}$ [48,51]. Compared to the CVs of Pt/C and Pd/C, no hydrogen underpotential desorption was observed on Au/C due to its weak adsorption ability. The ECSA of Pt/C was obtained from the hydrogen underpotential desorption peak, which was $41.5 \text{ m}^2 \text{ g}^{-1}$. The ECSAs of Pd/C and Au/C were calculated from their corresponding regions for reduction of a monolayer surface oxide, which were 48.3 and $24.2 \text{ m}^2 \text{ g}^{-1}$, for Pd/C and Au/C, respectively. Based on the charges transferred in their identical reaction regions, the active surface atom density was calculated by the following equation:

$$N_s = \frac{Q}{nFA} \quad (4)$$

Table 1
Summary of physical and electro-chemical properties of Pt/C, Pd/C, and Au/C catalysts.

| | Metal loading detected by ICP-AES | Diameter calculated from XRD (nm) | Diameter measured by TEM (nm) | ECSA ($\text{m}^2 \text{g}^{-1}$) | Active surface atom density (nmol cm^{-2}) |
|------|-----------------------------------|-----------------------------------|-------------------------------|-------------------------------------|---|
| Pt/C | 38% | 1.9 | 2.4 | 41.5 | 34.9 |
| Pd/C | 37% | 2.5 | 3.4 | 48.3 | 41.2 |
| Au/C | 35% | 3.4 | 3.5 | 24.2 | 26.2 |

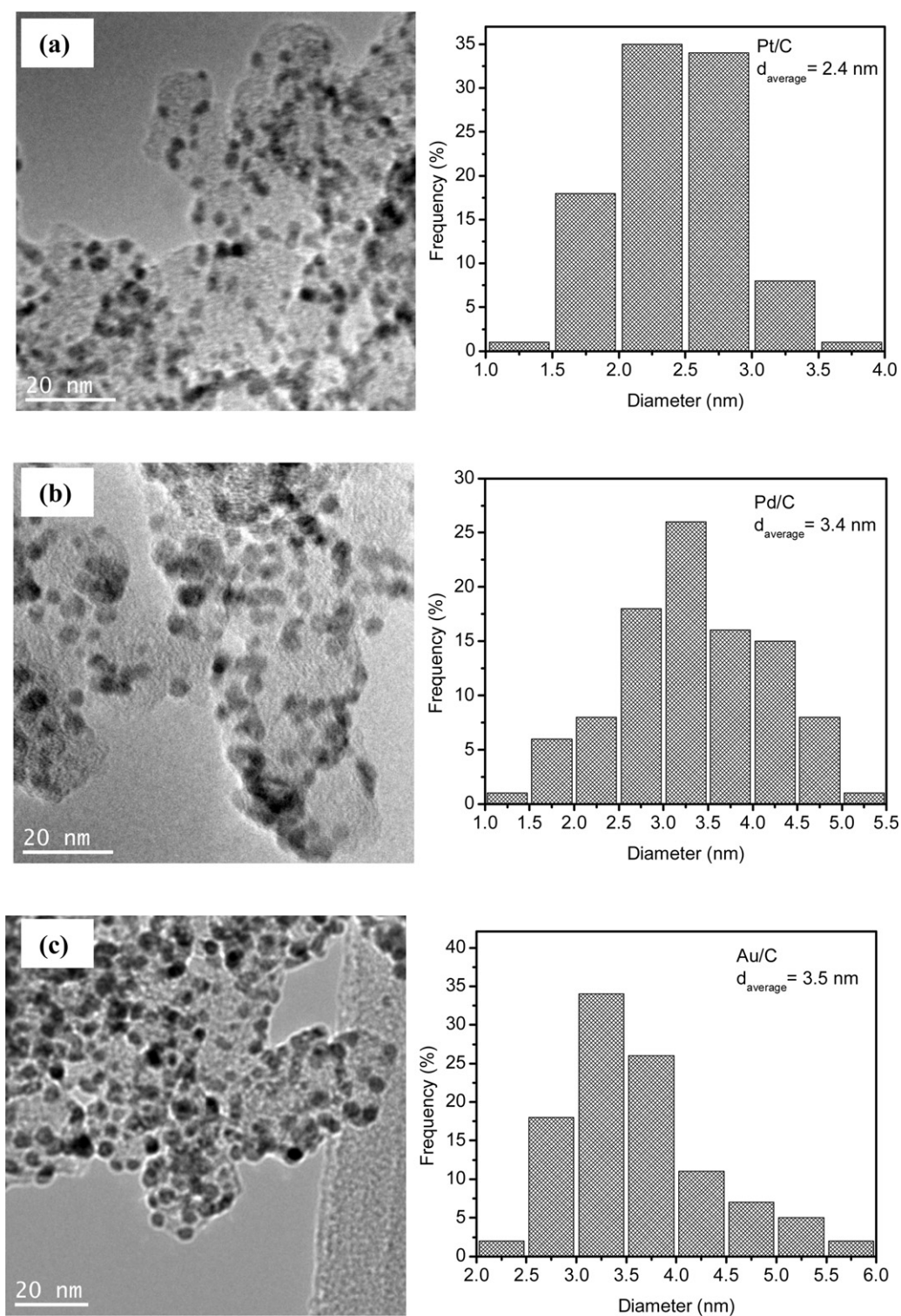


Fig. 2. TEM images and corresponding particle-size histograms of (a) Pt/C, (b) Pd/C, and (c) Au/C catalysts.

Table 2Onset potential, peak current density, Tafel slope, and αn on Pt/C, Pd/C, and Au/C catalysts at different temperature.

| | Pt/C | | | Pd/C | | | Au/C | | |
|---|-------|-------|-------|-------|-------|-------|-------|-------|-------|
| | 25 °C | 50 °C | 60 °C | 25 °C | 50 °C | 60 °C | 25 °C | 50 °C | 60 °C |
| Onset potential (mV) | −625 | −689 | −695 | −446 | −460 | −475 | −368 | −382 | −408 |
| Peak current density (mA cm ^{−2}) | 27.4 | 39.4 | 54.2 | 20.9 | 49.2 | 68.6 | 117.2 | — | — |
| Tafel slope | 145 | 108 | 102 | 88 | 88 | 85 | 134 | 127 | 127 |
| αn | 0.102 | 0.148 | 0.162 | 0.168 | 0.182 | 0.194 | 0.110 | 0.126 | 0.130 |

where N_s is the active surface atom density, Q is the total charge used for the ECSA calculation, n is the number of electrons involved in the reaction, F is Faraday's constant, and A is the geometric area of the glassy carbon electrode (0.1963 cm²). The number of electrons, n , is 1 for the hydrogen desorption reaction on Pt, and is 2 for the reduction of PdO. In the case of Au/C, it is reported that the monolayer oxide on Au surface is composed of AuO and Au(OH)₂ in alkaline electrolyte [52]. Therefore, n is 2 for the reduction of Au oxides. Based on Eq. (4), the active surface atom densities are 34.9, 41.2, and 26.2 nmol cm^{−2} for Pt/C, Pd/C, and Au/C, respectively.

Fig. 4 shows the CV profiles of glycerol oxidation in 1.0 M KOH + 0.5 M glycerol on Pt/C, Pd/C, and Au/C catalysts at 25 °C. Compared to the cyclic voltammograms in the blank KOH electrolyte (in Fig. 3.), the hydrogen adsorption/desorption peaks totally disappeared on Pt/C and Pd/C when glycerol was added into the electrolyte, indicating the surface active sites on these two catalysts were covered by the adsorbed glycerol or the corresponding intermediates. As the potential increased, the covered surface active sites were refreshed with the assistance of adsorbed OH, which resulted in the anodic peaks on Pt/C and Pd/C in the course of the forward scan. It is noted that a weak shoulder peak was observed at ~0.25 V on Pt/C in the forward scan, which is probably due to the glycerol oxidation on Pt oxide. Different from Pt/C and Pd/C, Au/C catalyst showed very little activity toward glycerol electro-oxidation at lower potentials. However, it demonstrated an extremely high peak current density at high potentials and a very broad active potential range [32,53]. This indicates that the Au catalyst can maintain its activity in a wide applied potential range. As demonstrated in our previous work, carbon nanotube supported Au can serve as a stable catalyst for the selective oxidation of glycerol to glycolate in an electro-catalytic reactor [40]. At the applied potential of 1.6 V vs. SHE, the Au/CNT anode electro-catalytic reactor yielded a glycolate of 85% at a glycerol conversion of 50%, after

a 6 h reaction. It is noted that at high potentials, the current density on Au/C became unstable. Previously, some authors assigned this instability to the complex kinetics of glycerol electro-oxidation on Au [51]. However, taking into consideration of the fast reaction rate under these high potentials, it is possibly due to the mass transfer issue, which leads to the insufficient supply of KOH and glycerol to the electrode surface. When comparing the polarization curves of these three catalysts, it is clear that at the low potential region (e.g. <0 V), Pt/C has the highest activity toward glycerol oxidation.

The glycerol electro-oxidations on these three catalysts were further investigated by linear sweep voltammetries in 1.0 M KOH + 0.5 M glycerol at different temperatures. A slow sweep rate of 1 mV s^{−1} and a rotation rate of 2500 rpm were applied to reduce the mass transfer/diffusion issue. As shown in Fig. 5(c), at 25 °C the unstable current observed on Au/C catalyst in Fig. 4 disappeared in this linear sweep, which evidenced that a better mass transfer was obtained. Therefore, it is reasonable to consider the reaction was taken place under quasi-steady state conditions. As presented in Fig. 5, temperature significantly facilitates glycerol electro-oxidation on these three catalysts. The onset potentials on these three catalysts (Table 2) moved to the negative position as the working temperature increasing from 25 °C to 60 °C. Meanwhile, the current density increased on all these catalysts across the whole potential range tested, indicating better kinetics were achieved at elevated temperatures. It is noted that at temperatures >50 °C, a shoulder peak appeared at ~−0.4 V on the Pt/C, which is probably due to the complex kinetics of glycerol oxidation. Investigations of HPLC analysis combined with half-cell voltammetry on both carbon supported Pt nanoparticle catalyst [31] and polycrystalline Pt electrode [54,55] have demonstrated that at room temperature (25 °C), glycerol is first oxidized to glycerate, which is then further oxidized to glycolate, tartronate, and oxalate. Increasing temperature may lead to complex reaction rate changes in these multi-step reactions

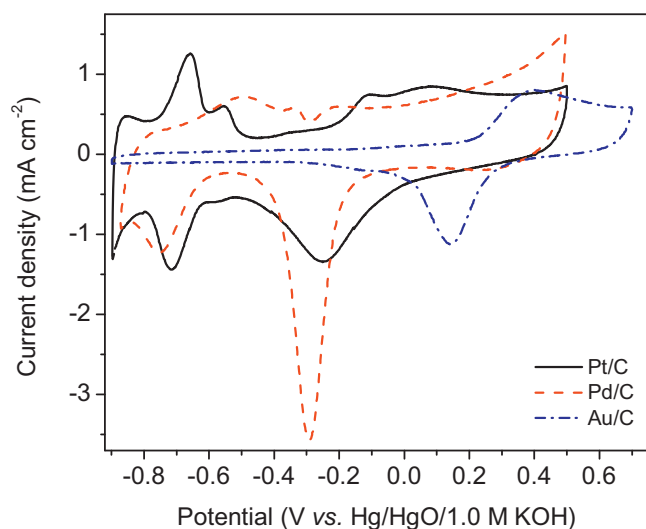


Fig. 3. Cyclic voltammograms of Pt/C, Pd/C, and Au/C catalysts in 1.0 M KOH, at 50 mV s^{−1}, 25 °C.

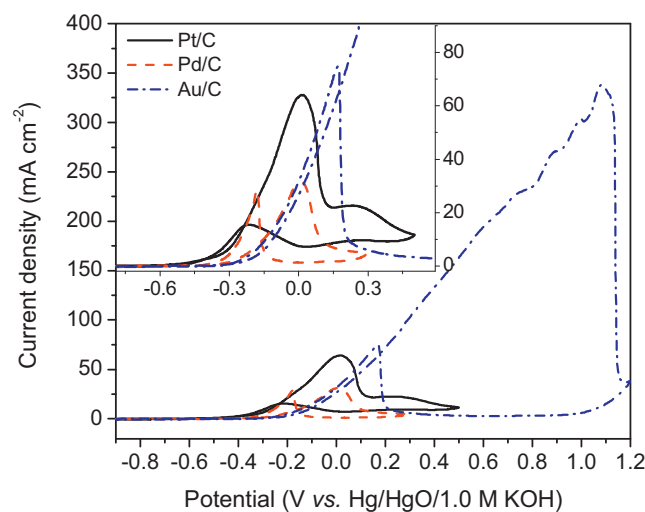


Fig. 4. Cyclic voltammograms of glycerol oxidation reaction on Pt/C, Pd/C, and Au/C catalysts in 1.0 M KOH + 0.5 M glycerol, 50 mV s^{−1}, 25 °C. The inserted graph shows the zoomed in parts from −0.7 V to 0.5 V.

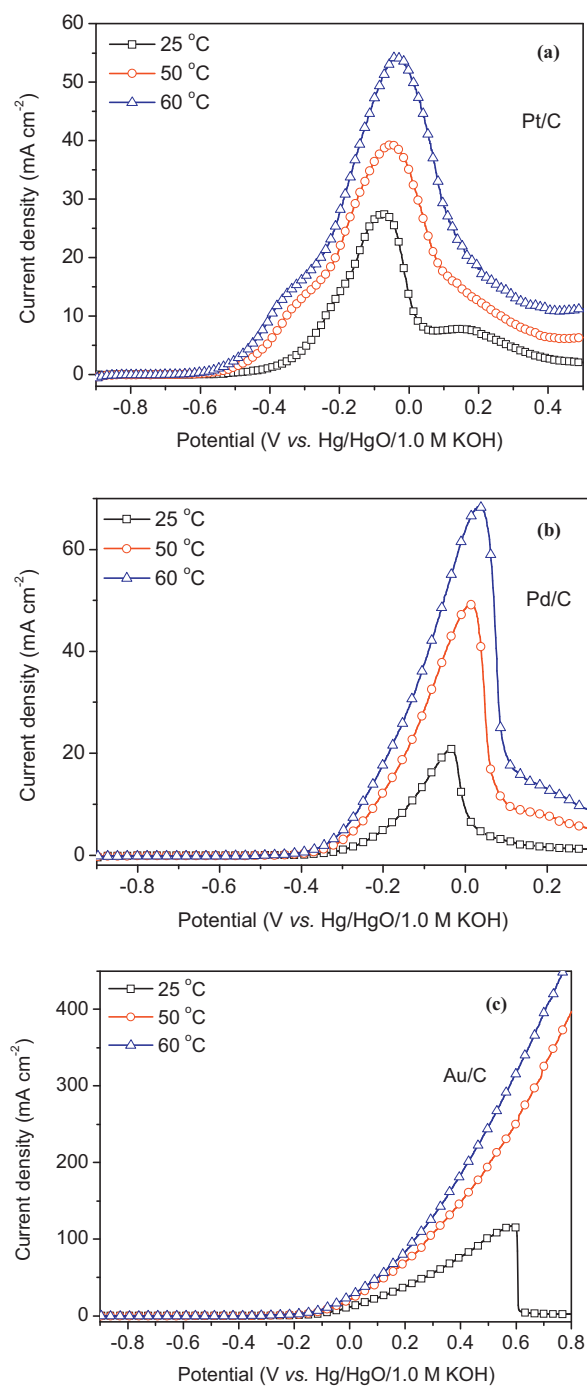


Fig. 5. Quasi-steady state linear scan voltammograms of glycerol oxidation on (a) Pt/C, (b) Pd/C, and (c) Au/C catalysts in 1.0 M KOH + 0.5 M glycerol, 1 mV s⁻¹, 2500 rpm, 25 °C.

and result in the formation of the shoulder peak. However, on Pd/C and Au/C catalysts, the polarization curves are similar in shape at all temperatures, indicating the reaction mechanisms on these two catalysts do not change significantly when temperature increases. It needs to be mentioned that at 25 °C, Pd/C has a higher onset potential, lower current density, and a narrower active potential region than Pt/C, which is probably due to the heavy poisoning from CO species on the Pd/C catalyst. As the reaction temperature was increased, the removal of these poisonous species on Pd/C was facilitated. As a result, at 60 °C, the peak current density increased to 68.6 mA cm⁻², which is even higher than the peak current density on Pt/C catalyst (54.2 mA cm⁻²). However, at low

potentials (e.g. < -0.1 V), the current density on Pt was still higher than that on Pd/C. Compared to Pt/C and Pd/C catalyst, Au/C has shown a much higher glycerol electro-oxidation activity at high potentials. Due to the highly stable nature of Au/C, the glycerol electro-oxidation peak at 25 °C was observed at ~0.59 V, with the peak current density at 117.2 mA cm⁻². The kinetics of glycerol electro-oxidation on Au/C was further facilitated at high temperatures. At temperatures > 50 °C (Fig. 5(c)), the anodic current density on Au/C continuously increased without any observation of peak current in the whole investigated potential range (-0.9–0.8 V).

To further compare the kinetic activities of Pt/C, Pd/C, and Au/C catalysts toward glycerol electro-oxidation, the Tafel plots at different temperature were investigated by plotting the potential versus the logarithm of current density, and the results are shown in Fig. 6. As the electro-oxidation of glycerol is a complicated reaction that may generate more than five possible stable oxygenates in alkaline electrolytes (glycerate, tartronate, mesoxalate, glycolate, oxalate, etc.) [16,31,40,55], the current density range for the Tafel plot investigation was chosen within 2 mA cm⁻² (<10% of the peak current density on Pd/C at 25 °C), in order to avoid the influences from deeper oxidized products. As shown in Fig. 6 and Table 2, within the investigated temperature of 25–60 °C, the Tafel plots on all these three catalysts follow linear trend lines, with the Tafel slopes in the range of 85–145 mV dec⁻¹. The comparable values of Tafel slope indicate that the glycerol electro-oxidation mechanisms in the low current density region should be similar on these three catalysts. The comparison of Tafel plots on different catalysts clearly shows that Pt/C needs an overpotential much lower than Pd/C and Au/C to obtain a certain current density, indicating that Pt/C holds the highest catalytic activity in this low potential range. The product of charge transfer coefficient and number of transferred electrons (αn) are also calculated and summarized in Table 2. As the temperature increasing, the products (αn) increased on all the catalysts, indicating the kinetics are greatly facilitated at higher temperatures.

Fig. 7 shows plots of the TOF of electrons as a function of potential in the low potential regions, which is estimated from Eq. (2). TOF is an absolute reaction rate, representing the number of electrons being transferred per unit time per catalyst surface active site. It directly reflects the intrinsic activity of the catalyst. It is clear that the TOF on all these catalysts increased as the potential and temperature increased. At low potentials, Pt atom demonstrated the highest activity based on the TOF plots at all the tested temperatures. At -0.4 V, the reaction rate per Pt atom (TOF) was 16 times higher than that per Pd atom at 25 °C, and was 23 times higher at 60 °C. At -0.3 V, the TOF on Pt is also 4–5 times higher than that on Pd and 20–30 times higher than that on Au at the tested temperatures.

3.3. Pt/C, Pd/C, and Au/C anode AEMFC with high purity glycerol

The performances of the AEMFCs with Pt/C, Pd/C, and Au/C anode catalysts were firstly studied with high purity glycerol fuel. As shown in Fig. 8, fed with 2.0 M KOH + 1.0 M glycerol, the Pt/C anode AEMFC demonstrated the highest performance at the cell operation temperature of both 50 °C and 80 °C, which is consistent with the Tafel plot and TOF investigations. The cell polarization curves on Pt/C anode are higher than that on Pd/C anode, and are much higher than that on Au/C anode over the whole current density range. At the fuel cell operation temperature of 50 °C (Fig. 8(a)), the open circuit voltage (OCV) observed on Pt/C anode AEMFC is 0.80 V, which is 0.07 V higher than that on Pd/C anode (0.73 V), and 0.19 V higher than that on Au/C (0.61 V). The OCV drop sequence is in good agreement with the half cell results, with Pt/C demonstrated the lowest onset potential (-689 mV) and Au/C demonstrated the highest one (-382 mV). Meanwhile, the peak power density obtained on Pt/C anode AEMFC was 58.6 mW cm⁻²,

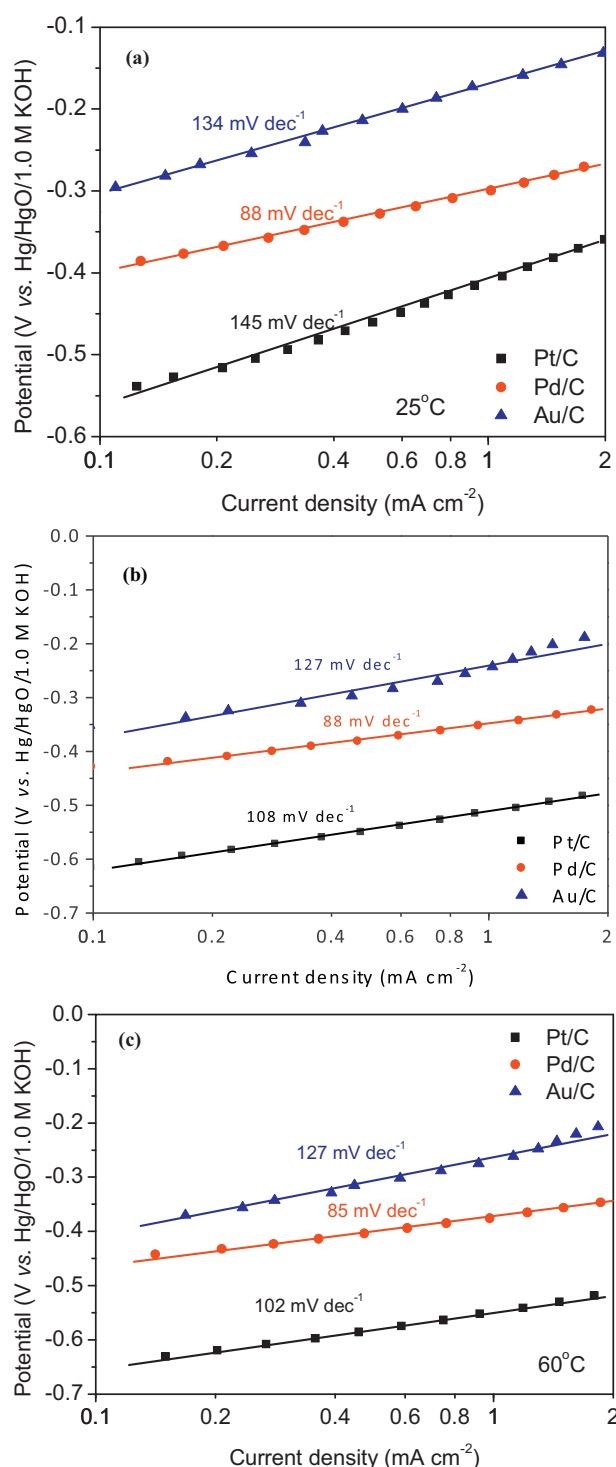


Fig. 6. Tafel plots of glycerol oxidation on Pt/C, Pd/C, and Au/C catalysts at (a) 25 °C, (b) 50 °C, and (c) 60 °C, in 1.0 M KOH + 0.5 M glycerol.

which is also much higher than the peak power density on Pd/C (37.4 mW cm^{-2}) and Au/C (17.8 mW cm^{-2}) anode AEMFCs. During the tests, the anode potentials were monitored through a Hg/HgO/1.0 M KOH reference electrode [16,31]. At the peak power densities, the anode potentials were ~ -0.45 , -0.40 , and -0.34 V on Pt/C, Pd/C, and Au/C anodes, respectively. The Tafel plot and TOF analyses obtained from half cell tests (shown in Figs. 6 and 7) also demonstrated that at the same temperature of 50 °C and the same potentials (-0.45 V for Pt/C, -0.40 V for Pd/C, and -0.34 V for Au/C),

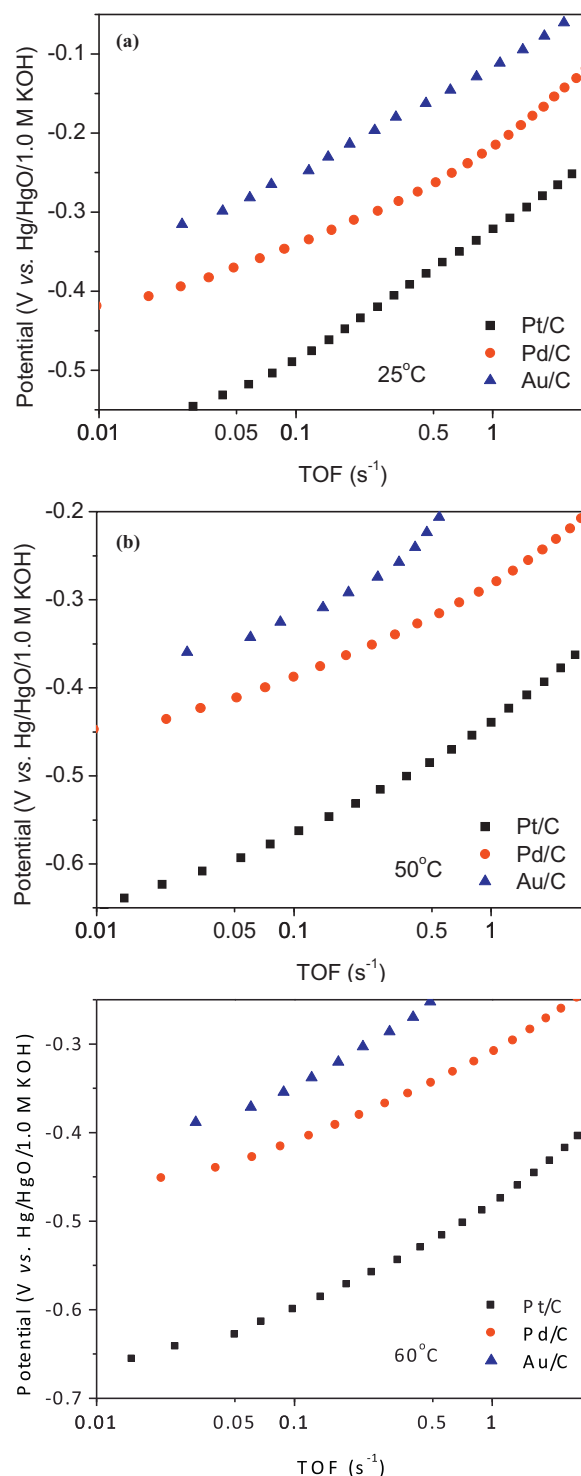


Fig. 7. Turnover frequencies (TOFs) of electrons for glycerol oxidation on Pt/C, Pd/C, and Au/C catalysts at (a) 25 °C, (b) 50 °C, and (c) 60 °C, in 1.0 M KOH + 0.5 M glycerol.

the Pt/C catalyst possessed the highest intrinsic activity toward glycerol oxidation in terms of both the current density and TOF of electrons. The results indicated good consistency between the half cell and single AEMFC tests. As the fuel cell operation temperature increased to 80 °C (Fig. 8(b)), it is clear that the performances over the whole tested current density range were greatly improved on all these catalysts. The peak power density of Pt/C anode AEMFC reached 124.5 mW cm^{-2} , which is two times greater than the peak power density at 50 °C (58.6 mW cm^{-2}). The peak power density

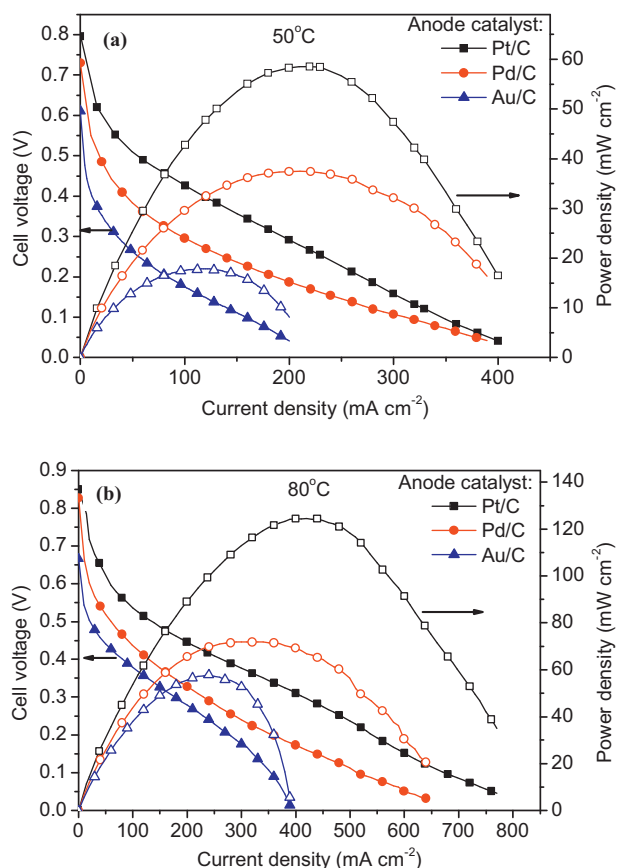


Fig. 8. Polarization and power density curves of Pt/C, Pd/C, and Au/C anode AEMFCs with high purity glycerol fuel at the operation temperature of (a) 50 °C and (b) 80 °C; anode fuel: 2.0 M KOH + 1.0 M high purity glycerol.

of Au/C anode AEMFC also showed a three-fold increase when the temperature increased from 50 °C to 80 °C. The higher performances of Pt/C, Pd/C, and Au/C anode AEMFC could be attributed to two aspects. First, the kinetics of both the anode and cathode reactions are enhanced at the elevated temperatures. The half cell investigations have demonstrated that for the glycerol oxidation reaction, both the αn and TOF greatly increases on all these three catalysts, while the onset potentials moves negatively. Meanwhile, the cathode ORR kinetics is also accelerated at higher operation temperatures. As a result, the OCVs of the AEMFCs with all these three anode catalysts increased at 80 °C. Second, the mass transfer is improved at higher temperatures. The conductivity of OH⁻ ion in the anion-exchange membrane (A201) increases with the increasing of the cell operation temperature, which significantly reduces the internal resistance [24]. In addition, the reactant diffusion is also better at higher temperature. Therefore, the mass transport limiting currents almost doubled on AEMFCs with all these three anode catalysts when the working temperature increased from 50 °C to 80 °C. It also needs to be mentioned that the peak power density on the monometallic Pt/C anode AEM-DGFC (124.5 mW cm⁻²) is comparable to the state-of-art direct methanol (168 mW cm⁻²) and ethanol (160 mW cm⁻²) AEMFCs with their optimized multi-metallic catalyst system (3 mg_{PtRu} cm⁻² for methanol and 1 mg_{Pd-(Ni-Zn-P)} cm⁻² for ethanol) and optimized experimental conditions (i.e. fuel composition flow rate, and temperature) [20,33]. The performances observed on Pt/C, Pd/C, and Au/C anode AEM-DGFCs are 2–3 orders of magnitude higher than that of current biofuel cells [56,57], and are also an order of magnitude higher than that of proton-exchange membrane direct glycerol fuel cells (PEM-DGFC) with PtRu/C anode

(4.0 mg_{PtRu} cm⁻²) and Pt/C cathode (4.0 mg_{Pt} cm⁻²) [31], indicating that glycerol serves as an efficient liquid fuel in AEMFCs.

3.4. Pt/C, Pd/C, and Au/C anode AEMFC with crude glycerol

Although glycerol demonstrates as a highly efficient fuel in AEMFCs, its wide application is heavily hurdled by the high cost of the high-purity glycerol fuel (ACS grade, which is usually applied in the academic research), even the price of industrial grade purified glycerol is still around 4–4.8 US\$ gal⁻¹. In contrast, the price of the 80–88% crude glycerol (after two simple steps of separation removing most of methanol, water, fatty acids, and unreacted oils) is only one sixth of the purified glycerol (0.74–0.89 US\$ gal⁻¹), which allow it serve as a more economical liquid fuel. However, it is concerning that the complicated components and multiple impurities may contaminate the fuel cell system and poison the anode catalyst. For example, the ash component may clog the pores of the liquid diffusion layer, the free fatty acids (soaps in alkaline solutions) would increase the liquid viscosity and adsorb on the catalyst surface, while the poisoning elements (Ca, Mg, Hg, P, S, and As) may also deactivate the anode catalysts. Therefore, up to now, all previous AEM-DGFC investigations were focused on the high purity glycerol fuel. No systematic work has been carried out to study the performance of AEMFC with biodiesel-derived crude glycerol.

In this work, the performances of Pt/C, Pd/C, and Au/C anode AEMFCs were further investigated with crude glycerol fuel at 80 °C. The soy biodiesel derived crude glycerol contains 88.05 wt% of glycerol, 5.42 wt% of matter organic non glycerol (MONG), 4.16 wt% of moisture, 2.37 wt% of ash, and 628 ppm methanol, and was used as purchased without any further treatment. As shown in Figs. 9 and 10, when 2.0 M KOH + 1.0 M crude glycerol was applied, the limiting current densities on AEMFCs with all the three anode catalyst dropped by ~100 mA cm⁻² than that obtained with high purity glycerol fuels (Fig. 8(b)) under the same testing conditions, indicating that the ashes and high viscosity MONG components (mainly soaps) will lead to a poor mass transfer phenomenon. Meanwhile, the comparison between Fig. 8(b) and Fig. 9(b) and (c) also shows that the crude glycerol fuel yielded lower OCVs and peak power densities on Pd/C and Au/C anode AEMFCs. Comparing to the results obtained with high purity glycerol (in Fig. 8(b)), fed with 2.0 M KOH + 1.0 M crude glycerol, the OCVs on Pd/C and Au/C anode AEMFCs dropped by 0.08 and 0.16 V, respectively, while the peak power density also reduced by 10.7 and 27.2 mW cm⁻², correspondingly. The drop in the performances with crude glycerol fuel may have risen from two aspects. First, the MONG components (methanol and soaps) in crude glycerol may block the active site on the surface of anode catalysts and lead to the loss in the overall performance. Second, the poisoning species may also be adsorbed on the catalysts and lead to the loss of its catalytic activity. Comparing to Au/C and Pd/C anode AEMFCs, it is interesting that both the OCV and the peak power density of Pt/C anode fuel cell show very little drop when switching from high purity glycerol to the crude glycerol fuel, which indicates the highly active Pt catalyst is also highly stable in this crude glycerol fuel cell system.

The effect of crude glycerol concentration on the AEMFCs with Pt/C, Pd/C, and Au/C was investigated by fixing the KOH concentration at 2.0 M, while increasing the crude glycerol concentration from 0.5 M to 5.0 M. The results were shown in Fig. 9. The OCVs summarized in Table 3 clearly demonstrated an increasing trend on fuel cells with all these anode catalysts, as the crude glycerol concentration increased. As is demonstrated in the half cell studies (Figs. 3 and 4), glycerol is adsorbed on Pt and Pd at very low potentials, and is further electrochemically oxidized at higher potentials with the assistance of adsorbed OH⁻ [15,48]. Therefore, in AEMFCs, the anode electrode potential on Pt/C and Pd/C catalysts are

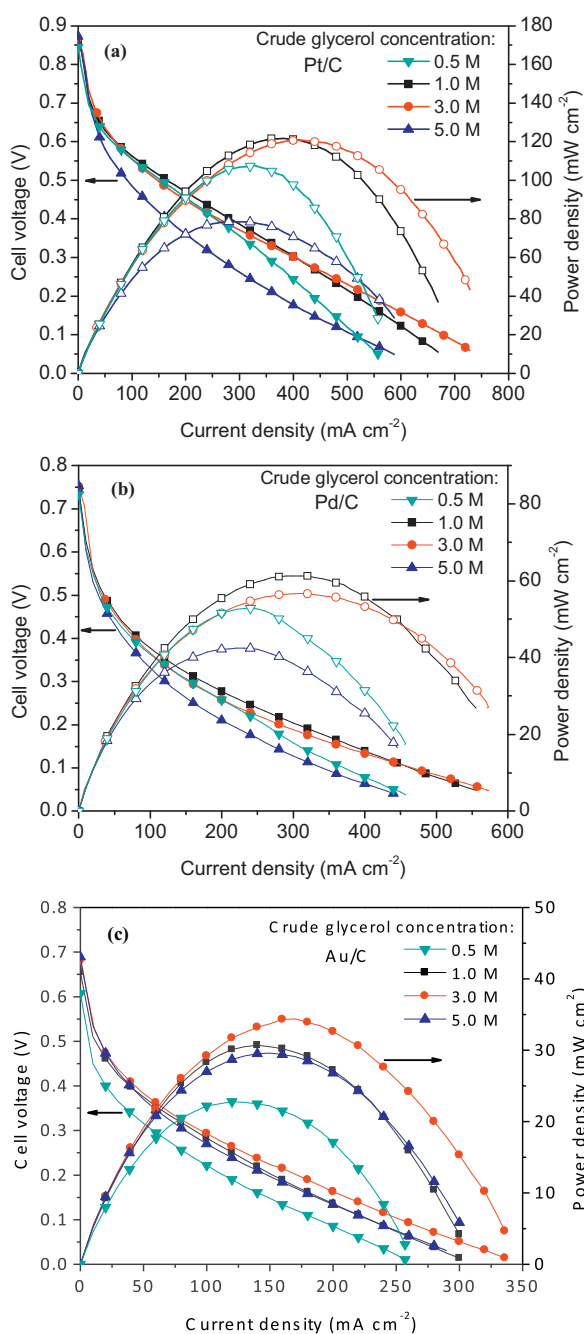


Fig. 9. Effect of crude glycerol concentration on fuel cell performances with (a) Pt/C, (b) Pd/C, and (c) Au/C anode catalysts, at 80 °C; KOH concentration: 2.0 M.

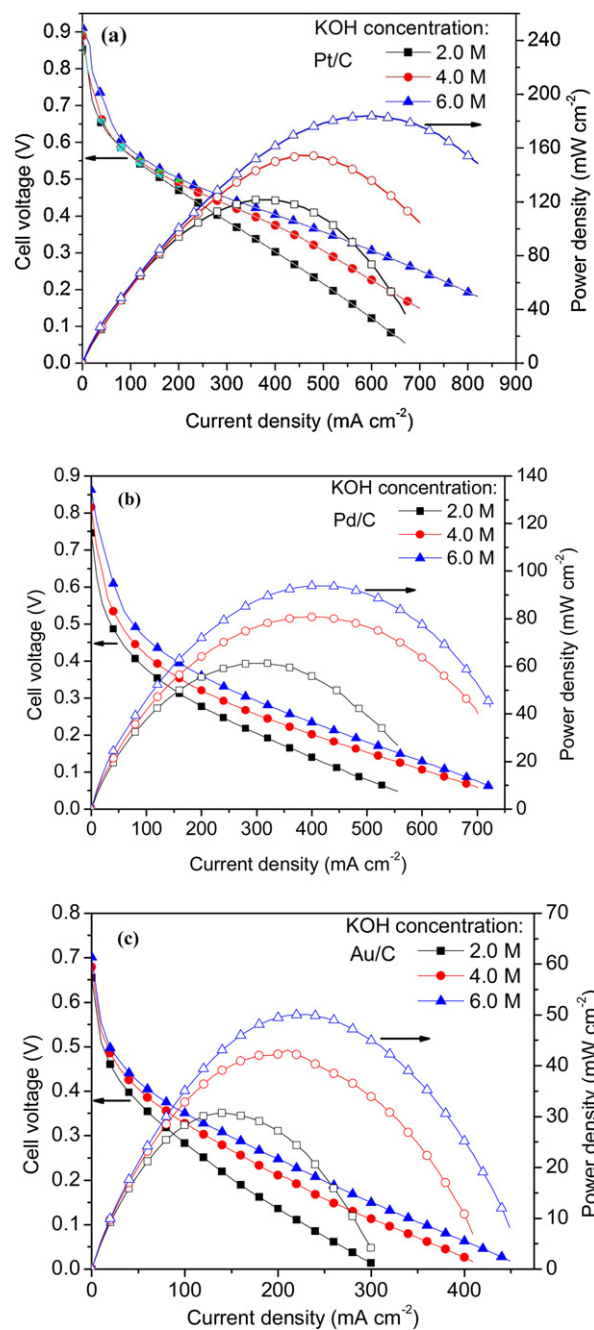


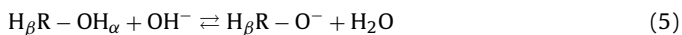
Fig. 10. Effect of KOH concentration on fuel cell performances with (a) Pt/C, (b) Pd/C, and (c) Au/C anode catalysts, at 80 °C; crude glycerol concentration: 1.0 M.

Table 3

Performances of AEMFCs with Pt/C, Pd/C, and Au/C anode and biodiesel derived crude glycerol fuel at 80 °C.

| KOH (M) | Crude glycerol (M) | Pt/C | | Pd/C | | Au/C | |
|---------|--------------------|---------|--|---------|--|---------|--|
| | | OCV (V) | Peak power density (mW cm^{-2}) | OCV (V) | Peak power density (mW cm^{-2}) | OCV (V) | Peak power density (mW cm^{-2}) |
| 2.0 | 0.5 | 0.845 | 107.7 | 0.733 | 52.8 | 0.607 | 22.8 |
| | 1.0 | 0.853 | 120.9 | 0.746 | 61.3 | 0.655 | 30.7 |
| | 3.0 | 0.867 | 121.0 | 0.752 | 56.6 | 0.680 | 34.4 |
| | 5.0 | 0.873 | 78.6 | 0.753 | 42.5 | 0.689 | 29.4 |
| 4.0 | 1.0 | 0.889 | 154.8 | 0.816 | 80.8 | 0.679 | 43.1 |
| 6.0 | | 0.911 | 184.2 | 0.863 | 93.9 | 0.701 | 50.1 |

governed by the catalyst surface coverage rate of both crude glycerol and OH. When the crude glycerol concentration increases, it will definitely reduce the adsorption of OH. At the OCV states, the electrode reaction rate is infinitely slow. The catalyst surface OH concentration can be maintained at an appropriate level. Therefore, when the crude glycerol concentration increased from 0.5 M to 5.0 M, a small increase in OCVs is still observed on Pt/C and Pd/C anode AEMFCs. For Au catalyst, the previous investigations have demonstrated that the alcohol electro-oxidation on Au depends on the formation of highly active alkoxide in the alkaline electrolyte [32,53]:



As glycerol is a weak acid with a $\text{pK}_a = 14.15$ [32], under the same pH value, higher glycerol concentrations will facilitate the formation of highly reactive glycerolate. Similar to the cases of Pt/C and Pd/C catalysts, the increasing of glycerolate concentration will favor its adsorption on the surface of Au catalyst and lead to a higher OCV on the Au/C anode AEMFC.

The peak power densities presented a volcano-type behavior against the crude glycerol concentration on all these three anode catalysts. The highest power densities were obtained with 3.0 M crude glycerol with Pt/C and Au/C anode catalysts, and 1.0 M crude glycerol with Pd/C catalyst. On one hand, the lower glycerol concentration will lead to lower coverage rate of glycerol on the surface of the catalysts (Pt and Pd) or lower concentration of the highly reactive glycerolate (Au), which further results in a lower performance. On the other hand, with a lower bulk glycerol concentration, the local glycerol concentration at the catalyst layer is restricted by the fuel delivery. When the reaction rate is fast enough, a glycerol concentration gradient was built up between the catalyst surface and the bulk electrolyte. Therefore, if the bulk glycerol concentration is low, at higher current density region, the insufficient supply of fuel to the catalyst layer will become a main limitation of the power output. This phenomenon is clearly observed on Pt/C and Pd/C anode AEMFC fed with 2.0 M KOH + 0.5 M crude glycerol. When the current density is greater than 250 mA cm^{-2} , the cell output voltage dropped faster with the increasing of current density, compared to the polarization curves with higher crude glycerol concentrations. However, due to the lower kinetics of glycerol electro-oxidation on Au/C, the mass transport issue is less important. Compared to lower glycerol concentrations, too high crude glycerol concentration will also lead to the decrease in AEMFC performance. As is explained above, the higher crude glycerol will lead to a lower OH coverage on Pt/C and Pd/C catalyst surfaces. When the anode potential deviates away from the OCV state, a lower coverage rate of OH will not be sufficient for the reaction, and consequently limit the AEMFC performance. Meanwhile, the products of glycerol oxidation (acids) need to be neutralized to salt form in the alkaline environment, which further consumes the OH^- in the catalyst layer. In addition, A higher crude glycerol concentration will increase the viscosity of the electrolyte, which will decrease the OH^- mobility, the release of products (in salt form) from the catalyst layer and increase the fuel cell internal resistance, leading to the drop of AEMFC performance [24,58,59].

The KOH effects on the AEMFC performance were investigated by fixing the crude glycerol concentration at 1.0 M, while increasing the KOH concentration from 2.0 M to 6.0 M, and are presented in Fig. 10. For Pt/C and Pd/C anode AEMFCs, the increasing of bulk KOH concentration will lead to a higher local OH^- concentration at the catalysts layer and a higher OH coverage on the catalyst surface, which will facilitate the glycerol oxidation. Therefore, as summarized in Table 3, the OCVs on both Pt/C and Pd/C anode AEMFCs increased at higher KOH concentrations. For Au/C, a higher pH of the electrolyte will lead to a higher concentration of glycerolate, leading to a higher OCV on Au/C anode AEMFC.

High KOH concentration will also facilitate the mass transfer in the system. Although it is reported that a higher KOH concentration will lead to the increase of internal resistance in an AEMFC [24,59], in our tested KOH concentration range (from 2.0 M to 6.0 M), we found the internal resistance was reduced at higher KOH concentration. When 2.0 M KOH was applied, the internal resistances on Pt/C, Pd/C, and Au/C anode AEMFCs were 150.9, 224.9, and $243.7 \text{ m}\Omega \text{ cm}^{-2}$, respectively, which reduced to 134.2, 151.9, and $227.4 \text{ m}\Omega \text{ cm}^{-2}$, respectively, when 6.0 M KOH was applied. In AEMFCs with liquid anode fuels, the internal resistance mainly rises from the membrane and the cathode, the resistances of which are related with their humidification. In our test, the anode was fabricated by airbrushing a thin layer of catalyst on the carbon cloth diffusion layer. Therefore, water from the anode liquid can easily penetrate into the thin AEM (28 μm), which allows the conducting of OH^- in the membrane under good humidification at all tested current densities. The cathode catalyst was directly airbrushed on the membrane to increase the contact at the interface. As a result, all the AEMFCs in our tests are observed with very low internal resistance. In addition, the higher KOH concentration will facilitate the release of the anode glycerol oxidation products and maintain the local pH in the catalyst layer during the current density region, both of which are better for both charge transfer and mass transfer at the anode. Consequently, when the KOH concentration increased from 2.0 M to 6.0 M (Fig. 10), the limiting current density on all the AEMFCs greatly increased. Due to the better kinetics and mass transfer, the performances were also greatly enhanced. Fed with 6.0 M KOH + 1.0 M glycerol, the peak power densities on Pt/C, Pd/C, and Au/C anode AEMFC reach 184.2, 93.9, and 50.1 mW cm^{-2} , respectively. These exciting results may open a new avenue to efficiently use biofuel waste crude glycerol as fuel for high performance anion exchange membrane fuel cells.

4. Conclusions

In this work, the carbon supported Pt (2.4 nm), Pd (3.4 nm), and Au (3.5 nm) nanoparticles with small average sizes and narrow size distributions were prepared through a modified nanocapsule method, and served as the model catalysts for the study of glycerol electro-oxidation and the performance of AEMFC with both high purity glycerol and biodiesel derived crude glycerol fuels. The half cell tests clearly demonstrated that Pt/C holds the highest activity in the low potential region, with a TOF 4–5 times higher than that on Pd and 20–30 times higher than that on Au at -0.3 V vs. $\text{Hg/HgO}/1.0 \text{ M KOH}$. The fuel cell investigation demonstrated that the Pt/C anode AEMFC can yield a peak power density of 124.5 mW cm^{-2} with 2.0 M KOH + 1.0 M high purity glycerol at 80°C , and amazingly did not show a drop in performance when the fuel was switched to the biodiesel derived crude glycerol (88 wt%), indicating high stability of the Pt/C anode AEMFC against the contamination/poisoning of the impurities in crude glycerol. Tests with different crude glycerol concentrations shows that an optimum crude glycerol concentration exists on Pt/C, Pd/C, and Au/C anode AEMFCs at a given KOH concentration, while at a given crude glycerol concentration, the fuel cell performance with all the three anode catalysts increases at higher KOH concentration. Fed with 6.0 M KOH + 1.0 M crude glycerol, the Pt/C anode AEMFC exhibits a very high power density of 184.2 mW cm^{-2} .

Acknowledgements

We acknowledge the US National Science Foundation (CBET-1159448) for funding. Acknowledgment is also made to the Research Excellence Fund – Research Seeds (REF-RS) grant

(E49290) from Michigan Tech for partial support of this research. Le Xin thanks a Michigan Tech Doctoral Finishing Fellowship and Ji Qi is grateful to the financial support from the Chinese Scholarship Council.

References

- [1] A.J. Ragauskas, C.K. Williams, B.H. Davison, G. Britovsek, J. Cairney, C.A. Eckert, W.J. Frederick, J.P. Hallett, D.J. Leak, C.L. Liotta, J.R. Mielenz, R. Murphy, R. Templer, T. Tschaplinski, *Science* 311 (2006) 484–489.
- [2] E.L. Kunkes, D.A. Simonetti, R.M. West, J.C. Serrano-Ruiz, C.A. Gärtner, J.A. Dumesic, *Science* 322 (2008) 417–421.
- [3] R.E. Smalley, Top ten Problems of Humanity for Next 50 Years, Energy & Nano Technology Conference, Rice University, 2003.
- [4] D.L. Klass, Biomass for Renewable Energy, Fuels, and Chemicals, Academic Press, San Diego, 1998.
- [5] BP, Statistical Review of World Energy June 2012, 2012.
- [6] <http://www.eia.gov/dnav/pet/hist/LeafHandler.ashx?n=pets&rwtc&f=d>.
- [7] B. Richter, D. Goldston, G. Crabtree, L. Glicksman, D. Goldstein, D. Greene, D. Kammen, M. Levine, M. Lubell, M. Savitz, D. Sperling, F. Schlachter, J. Scofield, J. Dawson, *Reviews of Modern Physics* 80 (2008) S1–S109.
- [8] L.B. Lave, *The Bridge* 39 (2009) 5–14.
- [9] M.S. Dresselhaus, I.L. Thomas, *Nature* 414 (2001) 332–337.
- [10] G.W. Huber, S. Iborra, A. Corma, *Chemical Reviews* 106 (2006) 4044–4098.
- [11] P.V. Kamat, *Journal of Physical Chemistry C* 111 (2007) 2834–2860.
- [12] C. Lamy, C. Coutanceau, J.-M. Leger, *Catalysis for Sustainable Energy Production*, Wiley-VCH Verlag GmbH & Co. KGaA, 2009, pp. 1–46.
- [13] E. Antolini, E.R. Gonzalez, *Journal of Power Sources* 195 (2010) 3431–3450.
- [14] E.H. Yu, U. Krewer, K. Scott, *Energies* 3 (2010) 1499–1528.
- [15] Z. Zhang, L. Xin, K. Sun, W. Li, *International Journal of Hydrogen Energy* 36 (2011) 12686–12697.
- [16] L. Xin, Z. Zhang, Z. Wang, W. Li, *ChemCatChem* 4 (2012) 1105–1114.
- [17] J.S. Spendelov, A. Wieckowski, *Physical Chemistry Chemical Physics* 9 (2007) 2654–2675.
- [18] S. Han, Y. Song, J. Lee, J. Kim, K. Park, *Electrochemistry Communications* 10 (2008) 1044–1047.
- [19] A. Santasalo-Aarnio, S. Hietala, T. Rauhala, T. Kallio, *Journal of Power Sources* 196 (2011) 6153–6159.
- [20] G.K.S. Prakash, F.C. Krause, F.A. Viva, S.R. Narayanan, G.A. Olah, *Journal of Power Sources* 196 (2011) 7967–7972.
- [21] J. Qi, L. Jiang, S. Wang, G. Sun, *Applied Catalysis B: Environmental* 107 (2011) 95–103.
- [22] S.Y. Shen, T.S. Zhao, J.B. Xu, Y.S. Li, *Energy & Environmental Science* 4 (2011) 1428–1433.
- [23] N. Fujiwara, Z. Siroma, S.I. Yamazaki, T. Ioroi, H. Senoh, K. Yasuda, *Journal of Power Sources* 185 (2008) 621–626.
- [24] Y.S. Li, T.S. Zhao, Z.X. Liang, *Journal of Power Sources* 187 (2009) 387–392.
- [25] A. Serov, C. Kwak, *Applied Catalysis B: Environmental* 97 (2010) 1–12.
- [26] L. Xin, Z. Zhang, J. Qi, D. Chadderton, W. Li, *Applied Catalysis B: Environmental* 125 (2012) 85–94.
- [27] K. Matsuoka, Y. Iriyama, T. Abe, M. Matsuoka, Z. Ogumi, *Journal of Power Sources* 150 (2005) 27–31.
- [28] V. Bambagioni, C. Bianchini, A. Marchionni, J. Filippi, F. Vizza, J. Teddy, P. Serp, M. Zhiani, *Journal of Power Sources* 190 (2009) 241–251.
- [29] C. Bianchini, P.K. Shen, *Chemical Reviews* 109 (2009) 4183–4206.
- [30] A. Ilie, M. Simoes, S. Baranton, C. Coutanceau, S. Martemianov, *Journal of Power Sources* 196 (2011) 4965–4971.
- [31] Z. Zhang, L. Xin, W. Li, *Applied Catalysis B: Environmental* 119/120 (2012) 40–48.
- [32] Z. Zhang, L. Xin, W. Li, *International Journal of Hydrogen Energy* 37 (2012) 9393–9401.
- [33] C. Bianchini, V. Bambagioni, J. Filippi, A. Marchionni, F. Vizza, P. Bert, A. Tampucci, *Electrochemistry Communications* 11 (2009) 1077–1080.
- [34] J. Van Gerpen, *Fuel Processing Technology* 86 (2005) 1097–1107.
- [35] D.T. Johnson, K.A. Taconi, *Environmental Progress* 26 (2007) 338–348.
- [36] J.C. Thompson, B.B. He, *Applied Engineering in Agriculture* 22 (2006) 261–265.
- [37] S.H. Sun, C.B. Murray, D. Weller, L. Folks, A. Moser, *Science* 287 (2000) 1989–1992.
- [38] W.Z. Li, Z.W. Chen, L.B. Xu, Y. Yan, *Journal of Power Sources* 195 (2010) 2534–2540.
- [39] Z. Zhang, K.L. More, K. Sun, Z. Wu, W. Li, *Chemistry of Materials* 23 (2011) 1570–1577.
- [40] Z. Zhang, L. Xin, J. Qi, Z. Wang, W. Li, *Green Chemistry* 14 (2012) 2150–2152.
- [41] Potentials of Common Reference Electrodes, <http://www.consultsr.com/resources/ref/refpots.htm>
- [42] L.D. Burke, J. Moran, P. Nugent, *Journal of Solid State Electrochemistry* 7 (2003) 529–538.
- [43] A.J. Bard, L.R. Faulkner, *Electrochemical Methods: Fundamentals and Applications*, 2nd ed., Wiley, New York, 2001.
- [44] U.A. Paulus, A. Wokaun, G.G. Scherer, T.J. Schmidt, V. Stamenkovic, V. Radmilovic, N.M. Markovic, P.N. Ross, *Journal of Physical Chemistry B* 106 (2002) 4181–4191.
- [45] O. Winjebi, Z.Y. Zhang, C.H. Liang, W.Z. Li, *Electrochimica Acta* 55 (2010) 4217–4221.
- [46] Z. Zhang, M. Li, Z. Wu, W. Li, *Nanotechnology* 22 (2011) 015602.
- [47] N.M. Marković, T.J. Schmidt, B.N. Grgur, H.A. Gasteiger, R.J. Behm, P.N. Ross, *The Journal of Physical Chemistry B* 103 (1999) 8568–8577.
- [48] L. Ma, D. Chu, R.R. Chen, *International Journal of Hydrogen Energy* 37 (2012) 11185–11194.
- [49] A.V. Tripkovic, K.D. Popovic, B.N. Grgur, B. Blizanac, P.N. Ross, N.M. Markovic, *Electrochimica Acta* 47 (2002) 3707–3714.
- [50] A.V. Tripkovic, S. Strbac, K.D. Popovic, *Electrochemistry Communications* 5 (2003) 484–490.
- [51] M. Simoes, S. Baranton, C. Coutanceau, *Applied Catalysis B: Environmental* 93 (2010) 354–362.
- [52] G. Tremiliosi-Filho, L.H. Dall'Antonia, G. Jerkiewicz, *Journal of Electroanalytical Chemistry* 422 (1997) 149–159.
- [53] Y. Kwon, S.C.S. Lai, P. Rodriguez, M.T.M. Koper, *Journal of the American Chemical Society* 133 (2011) 6914–6917.
- [54] Y. Kwon, M.T.M. Koper, *Analytical Chemistry* 82 (2010) 5420–5424.
- [55] Y. Kwon, K.J.P. Schouten, M.T.M. Koper, *Chemcatchem* 3 (2011) 1176–1185.
- [56] R.L. Arechederra, B.L. Treu, S.D. Minteer, *Journal of Power Sources* 173 (2007) 156–161.
- [57] R.L. Arechederra, S.D. Minteer, *Fuel Cells* 9 (2009) 63–69.
- [58] A. Verma, S. Basu, *Journal of Power Sources* 168 (2007) 200–210.
- [59] L. An, T.S. Zhao, S.Y. Shen, Q.X. Wu, R. Chen, *Journal of Power Sources* 196 (2011) 186–190.